RSC Advances

PAPER

View Article Online
View Journal | View Issue



Cite this: *RSC Adv.*, 2026, **16**, 26303

# Vibrational behaviors, piezoelectricity, spin-splitting, and carrier mobility in Janus HWSZ (Z = N, P, As) monolayers

A. I. Kartamyshev, [ab] Tuan V. Vu, [ab] A. A. Lavrentyev[c] and Nguyen D. Hien [*de]

Janus two-dimensional (2D) materials provide a versatile platform for symmetry-driven physics. However, the influence of surface functionalization on their intrinsic properties remains an open question. In this Letter, we propose and systematically investigate a class of Janus materials formed by the one-side hydrogenation of the Janus WSZ (Z = N, P, As) or HWSZ monolayers using first-principles density functional theory. Asymmetric hydrogenation acts as an additional symmetry-breaking mechanism, markedly reshaping the band structure and strengthening spin–orbit coupling. This transition yields a robust spin splitting up to 0.46 eV, highlighting the role of surface functionalization in engineering giant spin-dependent characteristics. Furthermore, the intrinsic vertical dipole induces a significant out-of-plane piezoelectric response, with the $d_{31}$ coefficient reaching 0.31 pm V$^{-1}$. In particular, we evaluate the electron mobility by explicitly incorporating multiple phonon scattering mechanisms to identify the fundamental transport limits.

Received 27th March 2026
Accepted 13th May 2026

DOI: 10.1039/d6ra02543a

rsc.li/rsc-advances



## 1 Introduction

The emergence of two-dimensional (2D) Janus materials has revolutionized the field of low-dimensional physics by breaking out-of-plane structural symmetry.[1,2] This intrinsic asymmetry produces a built-in dipole moment that enhances piezoelectric responses, enables sizable spin splitting, and accelerates carrier separation.[3,4] As a result, Janus systems exhibit properties that are fundamentally inaccessible in their centrosymmetric counterparts, making them attractive for next-generation nanoelectronic and optoelectronic devices.[5–7] Beyond their intrinsic characteristics, external modification strategies further expand the tunability of these materials. Among them, surface functionalization, particularly hydrogenation, has emerged as a powerful approach for modulating electronic phases, tailoring band structures, and even inducing magnetic behavior in 2D lattices.[8,9]

Although surface hydrogenation has been extensively investigated in symmetric monolayers such as graphene[10] and goldene,[6] its application to inherently asymmetric Janus structures introduces an additional and highly versatile degree of control. In symmetric systems, hydrogenation primarily modifies local bonding and opens band gaps; however, in Janus monolayers, it also interacts with the pre-existing intrinsic dipole field. By selectively hydrogenating one surface of a Janus structure, one can effectively tune the magnitude and direction of the internal electric field, thereby altering charge redistribution and interlayer potential gradients. This selective functionalization can significantly influence spin–orbit coupling (SOC), leading to enhanced Rashba-type spin splitting and enabling precise control over spin textures. Furthermore, hydrogen-induced modifications may stabilize new electronic or magnetic phases that are otherwise absent in pristine Janus materials. The coupling between chemical functionalization and structural asymmetry thus provides a rich platform for engineering material responses at the atomic scale. Consequently, the interplay between intrinsic Janus asymmetry and hydrogenation offers a highly flexible and controllable pathway for designing multifunctional materials with tailored electronic, transport, and spintronic properties, paving the way for innovative applications in quantum devices and energy technologies.

This study proposes and systematically investigates a class of functionalized 2D Janus systems, namely one-side hydrogenated Janus WSZ (Z = N, P, As) or HWSZ monolayers. Hydrogenation of an existing Janus material to create a new Janus structure represents a promising approach for exploring novel physical properties. Using density functional theory (DFT), we explore how the precise introduction of hydrogen on a specific

[a]*Laboratory for Computational Physics, Institute for Computational Science and Artificial Intelligence, Van Lang University, Ho Chi Minh City, Vietnam. E-mail: andrey.kartamyshev@vlu.edu.vn*

[b]*Faculty of Mechanical, Electrical, and Computer Engineering, Van Lang School of Technology, Van Lang University, Ho Chi Minh City, Vietnam. E-mail: tuan.vu@vlu.edu.vn*

[c]*Department of Electrical Engineering & Electronics, Don State Technical University, 344010 Rostov-on-Don, Russian Federation*

[d]*Institute of Research and Development, Duy Tan University, Da Nang 550000, Vietnam. E-mail: nguyendinhhien2@duytan.edu.vn*

[e]*School of Engineering & Technology, Duy Tan University, Da Nang 550000, Vietnam*

Janus surface acts as a secondary symmetry-breaking mechanism. Beyond simple surface passivization, this asymmetric hydrogenation modulates the intrinsic dipole moment of the WSZ template, providing a unique pathway to engineer its electronic band alignment. Our analysis focuses on the resulting modification of the electronic structure, vibrational behaviors, spin-dependent properties, and transport characteristics that arise from the interplay between the Janus-intrinsic field and hydrogen-induced perturbations. We primarily investigate the electronic properties of these monolayers, focusing on SOC-induced spin splitting and the emergence of out-of-plane piezoelectricity. A key aspect of this study is the rigorous evaluation of carrier mobility, carried out by explicitly incorporating multiple scattering mechanisms in order to elucidate the intrinsic limits of charge transport.

## 2 Computational details

First-principles calculations were carried out using the Vienna *Ab initio* Simulation Package (VASP). The projector augmented-wave (PAW) method[11,12] was employed to describe the core–valence interaction, and an energy cutoff of 650 eV was adopted for the plane-wave expansion. Electronic structures were evaluated using the Perdew–Burke–Ernzerhof (PBE)[13] and the hybrid Heyd–Scuseria–Ernzerhof (HSE06)[14] functionals. Further, spin–orbit coupling (SOC) was taken into consideration throughout the self-consistent electronic structure calculations.[15] Brillouin zone sampling employed a $12 \times 12 \times 1$ $\Gamma$-centered $k$-mesh, with convergence thresholds of $10^{-6}$ eV for energy and $10^{-3}$ eV Å$^{-1}$ for forces. A 25 Å vacuum layer and dipole-layer corrections were applied to eliminate periodic image interactions in the asymmetric Janus monolayers. Structural and thermal stabilities were verified *via* PHONOPY[16] with $5 \times 5 \times 1$ supercell and AIMD simulations at 300 K. Elastic and piezoelectric constants were derived using density functional perturbation theory (DFPT), while Raman spectra were calculated from the macroscopic dielectric tensor.[17] Carrier transport was modeled using AMSET package,[18] which accounts for multiple scattering mechanisms under the relaxation time approximation and integrates them *via* Matthiessen's rule.[19]

## 3 Results and discussion

The crystal structures of the proposed Janus HWSZ (Z = N, P, As) monolayers are shown in Fig. 1. The unit cell of HWSZ contains four atoms, consisting of one H, one W, one S, and one Z atom. Due to inherent vertical structural asymmetry, HWSZ crystallizes in the $P3m1$ space group. Structural optimization reveals that the in-plane lattice constants increase from 3.04 to 3.31 Å as the pnictogen elements changing from N to As. The calculated lattice constants and other structural parameters of the proposed Janus materials are summarized in Table 1.

To assess the structural stability of Janus HWSZ monolayers, the cohesive energy $E_{coh}$ was calculated first. This analysis is crucial for identifying viable candidates for experimental synthesis. The cohesive energy is defined by the following expression:

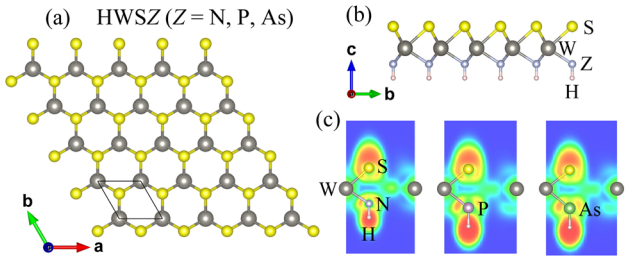


Fig. 1 Crystal structures (a and b) and electron localization function (c) of 2D Janus HWSZ (Z = N, P, As) monolayers. In the electron localization function maps, blue and red are used to represent charge depletion and charge accumulation, respectively.

$$E_{coh} = \frac{E_{tot} - (N_H E_H + N_W E_W + N_S E_S + N_Z E_Z)}{N_H + N_W + N_S + N_Z}, \quad (1)$$

where $E_{tot}$ represents the total energy of the Janus WHSZ monolayer, while $E_i$ and $N_i$ (i = H, W, S, Z) denote the energies of the isolated constituent atoms and their corresponding counts within the unit cell, respectively.

It is demonstrated that the obtained values of the cohesive energy for HWSN, HWSP, and HWSAs monolayers are −7.38, −6.57, and −6.18 eV, respectively. As a primary indicator of atomic bonding strength, a more negative cohesive energy signifies enhanced thermodynamic stability and stronger chemical bonds. Such significantly negative values indicate that these Janus monolayers are not only energetically favorable but also characterized by strong chemical bonds, ensuring their structural and thermodynamic stability. Further, to elucidate the chemical bonding in the Janus HWSZ monolayers, we also performed a Bader charge analysis to quantify charge transfer among atoms. Owing to the structural asymmetry and electronegativity differences, this analysis is crucial for understanding the origin of the internal dipole moment. The Bader charge analysis results for all three Janus structures are presented in Table 1. It is evident that the W atoms lose a significant amount of charge across all three structures. This is attributed to the fact that the electronegativity of W is considerably lower than that of S and N, and only marginally higher than that of P and As (W bonded to S and Z = N, P, As). In the case of Z = N, namely HWSN monolayer, charge strongly accumulates around the N atoms due to its high electronegativity. In contrast, the pnictogen elements P and As act as charge donors in the cases of HWSP and HWSAs owing to their lower electronegativity relative to the surrounding atoms. The calculated electron localization function of the studied structures are also provided in Fig. 1. The asymmetric charge transfer inherent in Janus configurations induces an intrinsic dipole moment across the layer, creating a shift in vacuum levels within the electrostatic potential. To gain deeper insight, we analyzed the planar-averaged electrostatic potential, as shown in Fig. 2, to evaluate the difference between the vacuum levels and determine the corresponding work functions of the Janus monolayers. A pronounced difference in vacuum levels exists between the two surfaces, with values of 2.70, 2.20, and 2.29 eV for HWSN, HWSP, and HWSAs monolayers, respectively,as listed in Table

Table 1 Lattice constants $a$ (Å), bond lengths $d$ (Å), monolayer thicknesses $\Delta h$ (Å), cohesive energies $E_{coh}$ (eV per atom), and Bader charge analysis results $q(e)$, vacuum level difference $\Delta\Phi$ (eV), and work functions $\Phi_{H,S}$ (eV) of Janus HWSZ (Z = N, P, As) monolayers

| | $a$ | $d_{S-W}$ | $d_{W-Z}$ | $d_{Z-H}$ | $\Delta h$ | $E_{coh}$ | $q_W$ | $q_H$ | $q_S$ | $q_Z$ | $\Delta\Phi$ | $\Phi_H$ | $\Phi_S$ |
|---|---|---|---|---|---|---|---|---|---|---|---|---|---|
| HWSN | 3.04 | 2.38 | 2.10 | 1.03 | 3.78 | −7.38 | −1.217 | 0.024 | 0.370 | 0.823 | 2.70 | 2.70 | 5.40 |
| HWSP | 3.26 | 2.43 | 2.39 | 1.42 | 4.43 | −6.57 | −0.812 | 0.519 | 0.473 | −0.180 | 2.20 | 2.99 | 5.19 |
| HWSAs | 3.31 | 2.44 | 2.48 | 1.52 | 4.60 | −6.18 | −0.586 | 0.485 | 0.466 | −0.365 | 2.29 | 3.03 | 5.32 |

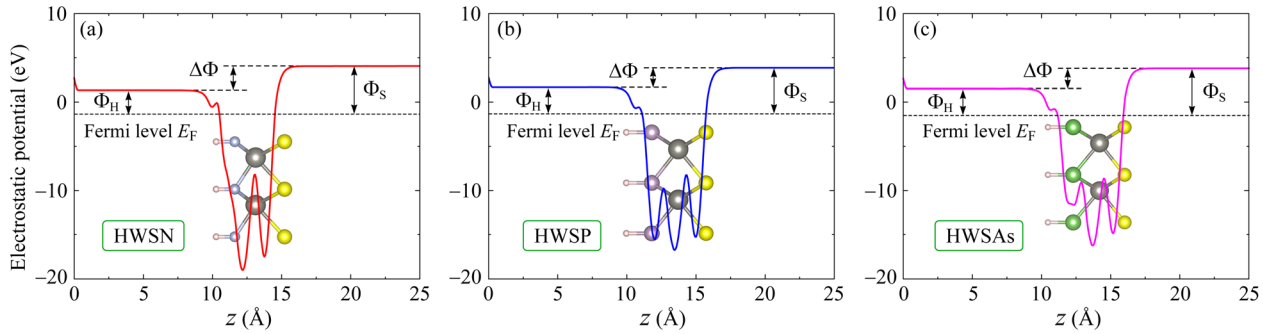


Fig. 2 Planar-averaged electrostatic potentials of 2D Janus HWSN (a), HWSP (b), and HWSAs (c) monolayers.

1. The work function $\Phi$, defined from the Fermi level $E_F$ and the vacuum level $E_{vac}$ according to $\Phi = E_{vac} - E_F$, varies across the two surfaces. As shown in Table 1, the work function at the S-terminated surface $\Phi_S$ is significantly larger than at the H-terminated surface $\Phi_H$, indicating that electrons can be more easily extracted from the H-terminated face.

To thoroughly evaluate the dynamic behavior and thermal stability of the investigated structures, AIMD simulations were executed at a constant room temperature over a trajectory of 10 ps. As illustrated in Fig. 3, the evolution of the total energy displays merely marginal variations, confined to a narrow energetic window of around 0.5 eV over the entire simulated timeframe. This steady energetic profile strongly implies that the atomic configurations continuously oscillate around their local thermodynamic minima without escaping the equilibrium state. Crucially, a detailed examination of the final atomic coordinates demonstrates that the proposed structures perfectly maintain their intrinsic lattice integrity. Also, there are no observable indications of critical failures such as bond breaking, surface reconstruction, or spontaneous transition into alternate structural phases. Ultimately, this combination of conserved atomic topology and steady thermodynamic parameters unequivocally confirms the excellent thermal durability of these materials under ambient environmental conditions, highlighting their potential for room-temperature device integration.

Next, we calculate the phonon dispersion spectra of the materials to evaluate their vibrational behaviors and, specifically, to assess their dynamical stability. Fig. 4(a) displays the phonon spectra of HWSZ, which consists of 12 phonon branches: three acoustic branches in the low-frequency region and nine optical branches at higher frequencies. A significant gap is observed within the optical vibration region, which can be attributed to the contrast in atomic sizes between the constituent elements (specifically between H and the other components). Most importantly, the absence of imaginary modes throughout the Brillouin zone confirms the dynamical stability of the proposed crystal structures.

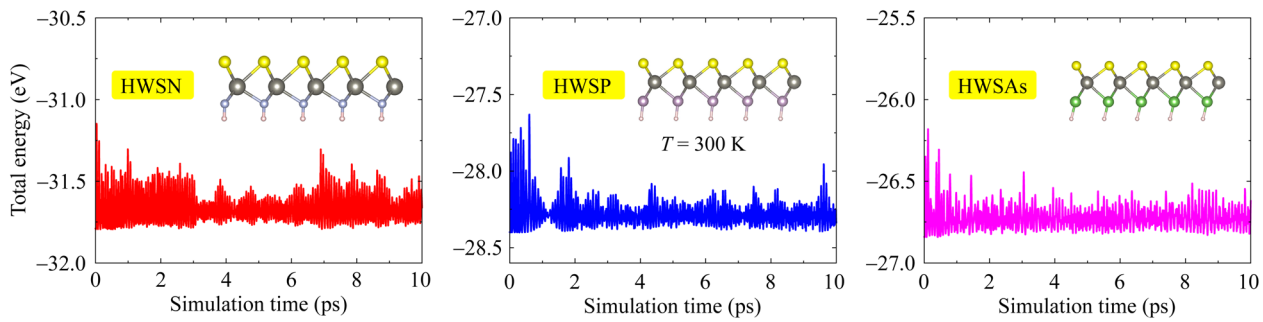


Fig. 3 Time-dependent total energy variations during room-temperature AIMD simulations of HWSZ (Z = N, P, As) monolayers. The insets within panels illustrate the final snapshots of the crystal structures at the end of the simulation.

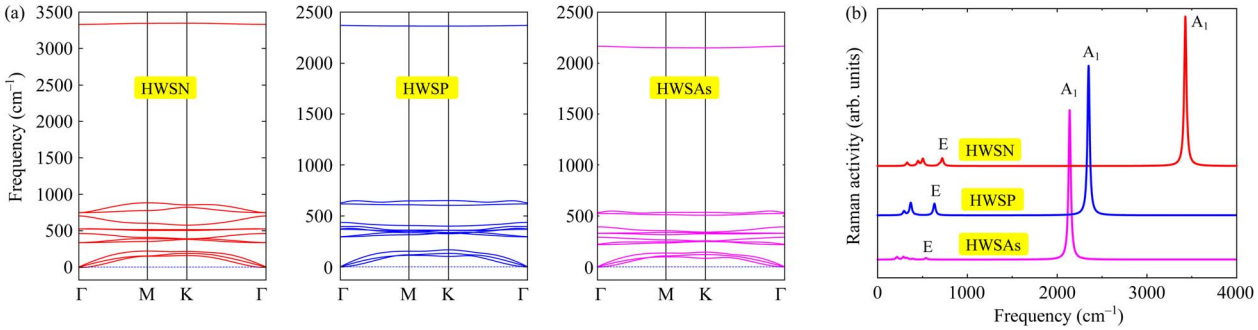


Fig. 4 (a) Phonon dispersions and (b) Raman activities of Janus HWSZ (Z = N, P, As) monolayers.

While our structural analyses confirm the theoretical stability of the proposed HWSZ (Z = N, P, As) monolayers, establishing their experimental feasibility is equally crucial for future applications. Drawing inspiration from the successful synthesis of Janus transition metal dichalcogenides[1] and Janus graphene with one-side functionalization,[10] we propose a highly plausible two-step fabrication strategy. First, the foundational WSZ Janus structure can be synthesized *via* chemical vapor deposition (CVD) coupled with selective atomic substitution. Subsequently, asymmetric hydrogenation can be achieved using a controlled hydrogen plasma treatment, a technique widely proven to be effective for the surface functionalization of other 2D materials.[20] Together, these steps provide a robust and viable pathway for experimental realization.

To further investigate the vibrational properties and provide a reference for experimental characterization, we calculated the Raman active modes of the Janus monolayer. For the structure crystallizing in the *P*3*m*1 space group with a four-atom unit cell, group theory analysis predicts a specific set of Raman-active vibrations. At the Brillouin zone center ($\Gamma$), the total representation of the optical phonon modes can be decomposed into irreducible representation as $3A_1 + 3E$, where both the $A_1$ (non-degenerate) and E (doubly degenerate) modes are Raman active. The $A_1$ modes correspond to out-of-plane vibrations, while the E modes represent in-plane displacements. For crystals belonging to the *P*3*m*1 space group, both $A_1$ and E modes exhibit Raman activity. The distinct peaks observed in the calculated Raman spectrum serve as a fingerprint for identifying the structural integrity and the broken inversion symmetry of the Janus lattice. The Raman spectra presented in Fig. 4(b) show that the Raman peak corresponding to the $A_1$ mode at the highest optical vibrational frequency exhibits a remarkably strong intensity, substantially exceeding that of all other Raman features. Other Raman-active modes are also clearly resolved, with particularly pronounced contributions from the high-frequency E modes, such as the E peak at 720 cm$^{-1}$ in the HWSN monolayer and the E peak at 633 cm$^{-1}$ in the HWSP monolayer.

Beyond dynamical stability, we evaluated the mechanical integrity of the monolayers through their elastic constants. Due to their hexagonal symmetry, the mechanical response of Janus HWSZ is fully defined by the in-plane constants $C_{11}$, $C_{12}$, and $C_{66}$, where $C_{66} = (C_{11} - C_{12})/2$. These parameters determine the mechanical stability criteria and also in-plane stiffness. From these values, the Young's modulus and Poisson's ratio were calculated to comprehensively characterize the mechanical strength and flexibility of the studied 2D structures. The calculated results for the in-plane elastic constants of HWSZ monolayers are summarized in Table 2. It is demonstrated that the calculated $C_{11}$ elastic constants are relatively high, varying from 109.92 to 188.95 N m$^{-1}$, while the corresponding $C_{12}$ values are considerably lower, in the range of from 23.75 to 41.57 N m$^{-1}$. The positive values of $C_{66}$ across all three proposed structures signify robust shear rigidity, a prerequisite for maintaining structural integrity under tangential stress. These calculated values satisfy the Born criteria, specifically $C_{11} > 0$ and $C_{11} > |C_{12}|$,[21,22] thereby confirming that all three structures are mechanically stable and resistant to spontaneous deformation. The calculated Young's modulus values $Y_{2D}$ exhibit a systematic decline as the atomic size of the pnictogen species increases, shifting from 179.80 N m$^{-1}$ for HWSN to 104.79 N m$^{-1}$ for HWSAs. This downward trajectory indicates a pronounced mechanical softening trend, where the substitution of nitrogen with heavier pnictogens like phosphorus and

Table 2 Calculated elastic constants $C_{ij}$, Young's modulus $Y_{2D}$, Poisson's ratio $\nu_{2D}$, piezoelectric coefficients $e_{ij}$ and $d_{ij}$, PBE/HSE06/PBE + SOC band gaps $E_g$, and spin splitting energy at *K* point in the valence band $\lambda_v$ of Janus HWSZ monolayers

| | $C_{11}$ (N m$^{-1}$) | $C_{12}$ (N m$^{-1}$) | $C_{66}$ (N m$^{-1}$) | $Y_{2D}$ (N m$^{-1}$) | $\nu_{2D}$ | $e_{11}$ ($10^{-10}$ C m$^{-1}$) | $e_{31}$ ($10^{-10}$ C m$^{-1}$) | $d_{11}$ (pm V$^{-1}$) | $d_{31}$ (pm V$^{-1}$) | $E_g^{PBE}$ (eV) | $E_g^{HSE06}$ (eV) | $E_g^{PBE+SOC}$ (eV) | $\lambda_v$ (eV) |
|---|---|---|---|---|---|---|---|---|---|---|---|---|---|
| HWSN | 188.95 | 41.57 | 73.69 | 179.80 | 0.22 | 2.59 | 0.71 | 1.76 | 0.31 | 2.17 | 2.67 | 1.93 | 0.43 |
| HWSP | 120.70 | 24.30 | 48.20 | 115.81 | 0.20 | 3.96 | −0.23 | 4.11 | 0.16 | 1.38 | 1.80 | 1.13 | 0.45 |
| HWSAs | 109.92 | 23.75 | 43.09 | 104.79 | 0.22 | 4.41 | −0.41 | 5.12 | −0.31 | 1.30 | 1.72 | 1.03 | 0.46 |

arsenic weakens the interatomic resistance to elastic deformation. This phenomenon is likely driven by the increase in bond lengths and the corresponding reduction in orbital overlap associated with larger atomic radii. The stiffness values of the HWSZ monolayers are comparable to those of several similar structures, such as $WSiAs_3H$ (124.80 N $m^{-1}$)[23] or $WBAsS_2$ (195.93 N $m^{-1}$).[24] However, these values are still significantly lower than that of graphene (336 N $m^{-1}$).[25] The Janus HWSZ monolayers exhibit a consistent Poisson's ratio ($\nu_{2D} \approx 0.2$ as listed in Table 2), indicating relatively low lateral contraction under uniaxial tensile strain. This stability across the series suggests that the fundamental bonding nature and elastic anisotropy are preserved, even as in-plane stiffness decreases with larger pnictogen atomic sizes. Ultimately, a Poisson's ratio of 0.2 reflects an ideal balance between mechanical rigidity and flexibility, ensuring structural integrity and a low risk of instability under moderate strain.

Having established the mechanical behavior of these monolayers through their elastic constants, we now shift our focus to the piezoelectric coefficients to evaluate their electromechanical coupling and response. The intrinsic lack of inversion symmetry in 2D Janus materials gives rise to pronounced structural anisotropy, thereby enabling both in-plane and out-of-plane piezoelectric responses. Here, we employ a DFT-based approach to calculate the piezoelectric coefficients, as proposed previously by Duerloo and co-workers.[26] The piezoelectric tensors $e_{ijk}$ and $d_{ijk}$ are defined according to the following relations:[26,27]

$$e_{ijk} = \frac{\partial P_i}{\partial \varepsilon_{jk}}, \tag{2}$$

$$d_{ijk} = \frac{\partial P_i}{\partial \sigma_{jk}}. \tag{3}$$

where $P_i$ denotes the polarization component, $\varepsilon_{jk}$ and $\sigma_{jk}$ represent the strain and stress tensors, respectively. The indices ($i, j, k = 1, 2, 3$) correspond to the Cartesian directions, with 1, 2, and 3 indicating the $x$, $y$, and $z$ axes, respectively. In the case of 2D Janus monolayers, the piezoelectric coefficients $e_{11}$ and $e_{31}$ can be directly calculated using the DFT method, while the corresponding $d_{ij}$ coefficients can be obtained from the following relations:[27]

$$d_{11} = \frac{e_{11}}{C_{11} - C_{12}}, \tag{4}$$

$$d_{31} = \frac{e_{31}}{C_{11} + C_{12}}. \tag{5}$$

The calculated results for the piezoelectric coefficients of Janus HWSZ monolayers are summarized in Table 2. The values of $e_{11}$ for Janus HWSZ are found to range from $2.59 \times 10^{-10}$ to $4.41 \times 10^{-10}$ C $m^{-1}$, while the absolute values of $e_{31}$ lie between $0.23 \times 10^{-10}$ to $0.71 \times 10^{-10}$ C $m^{-1}$. Meanwhile, Janus WHSAs exhibits the highest in-plane piezoelectric response, exhibits the highest in-plane piezoelectric response, with a $d_{11}$ value of 5.12 pm $V^{-1}$. The corresponding $d_{11}$ values for Janus HWSN and HWSP are calculated to be 1.76 and 4.11 pm $V^{-1}$, respectively. These obtained values are significantly higher than those reported for several similar structures, such as $MSi_2N_4$ (0.778 pm $V^{-1}$),[28] $MoSiN_3H$ (1.622 pm $V^{-1}$),[29] and $WSiN_3H$ (0.99 pm $V^{-1}$).[23] The large $d_{11}$ value of WHSAs is comparable to that of several structures exhibiting strong in-plane piezoelectric effects, such as $In_2SeTe$ (4.73 pm $V^{-1}$)[27] and NiClI (5.12 pm $V^{-1}$).[30] Notably, the Janus HWSZ monolayers exhibit remarkable out-of-plane piezoelectric coefficient $d_{31}$, reaching up to 0.31 pm $V^{-1}$ (in absolute value) for both HWSN and HWSAs monolayers. The out-of-plane piezoelectric response of these HWSZ monolayers is comparable to that of several other 2D materials with pronounced piezoelectric properties, such as Janus $GaInS_2$ ($d_{31}$ = 0.38 pm $V^{-1}$).[27] This substantial vertical response, characteristic of Janus structures, confers multifunctional potential upon the monolayers, making them promising candidates for integration into advanced electromechanical and sensing applications.

We next explore the electronic properties of the proposed Janus HWSZ monolayers, which are crucial for understanding their fundamental physics and evaluating their potential for technological applications. The calculated band structures of HWSZ materials are presented in Fig. 5. Obtained results are indicated that all three Janus structures are semiconductors with direct band gaps at $K$ point in the Brillouin zone. At the PBE theoretical level, the band gaps of HWSN, HWSP, and HWSAs are found to be 2.17, 1.38, and 1.30 eV, respectively. The correction of the band structures using the HSE06 hybrid functional leads to a significant increase in the band gaps compared to the PBE results, as shown in Fig. 5(a). Accordingly, the corrected band gap energies of the Janus HWSZ monolayers are found to range from 1.72 to 2.67 eV, as summarized in Table 2. Further, we also evaluate the influence of SOC on the electronic bands of the proposed Janus structures. It is indicated that SOC is essential for an accurate description of electronic properties, particularly in systems containing heavy elements like tungsten. In such materials, these relativistic effects significantly modify the band structure by lifting degeneracies and shifting energy levels, which in turn alters the fundamental electronic characteristics of materials. The calculated band structures by PBE + SOC method for Janus HWSZ monolayers are shown in Fig. 5(b). The inclusion of SOC slightly reduces the band gap energies of the proposed Janus materials, as detailed in Table 2. Notably, SOC lifts the spin degeneracy, resulting in distinct spin-split energy levels throughout the band structure. A pronounced spin splitting occurs within the valence band at the $K$-point, where the splitting energy $\lambda_v$ reaches a significant magnitude of 0.46 eV (HWSAs).

Finally, we evaluate the carrier mobility of the proposed Janus HWSZ structures. Various scattering mechanisms have been taken into account, including acoustic-deformation-potential (ADP), ionized-impurity (IMP), piezoelectric (PIE), and polar-optical-phonon (POP) scattering. The total mobility $\mu_{total}$ is determined *via* Matthiessen's rule, including the contributions of these individual mechanisms:[19]

$$\frac{1}{\mu_{total}} = \frac{1}{\mu_{ADP}} + \frac{1}{\mu_{IMP}} + \frac{1}{\mu_{PIE}} + \frac{1}{\mu_{POP}}, \tag{6}$$

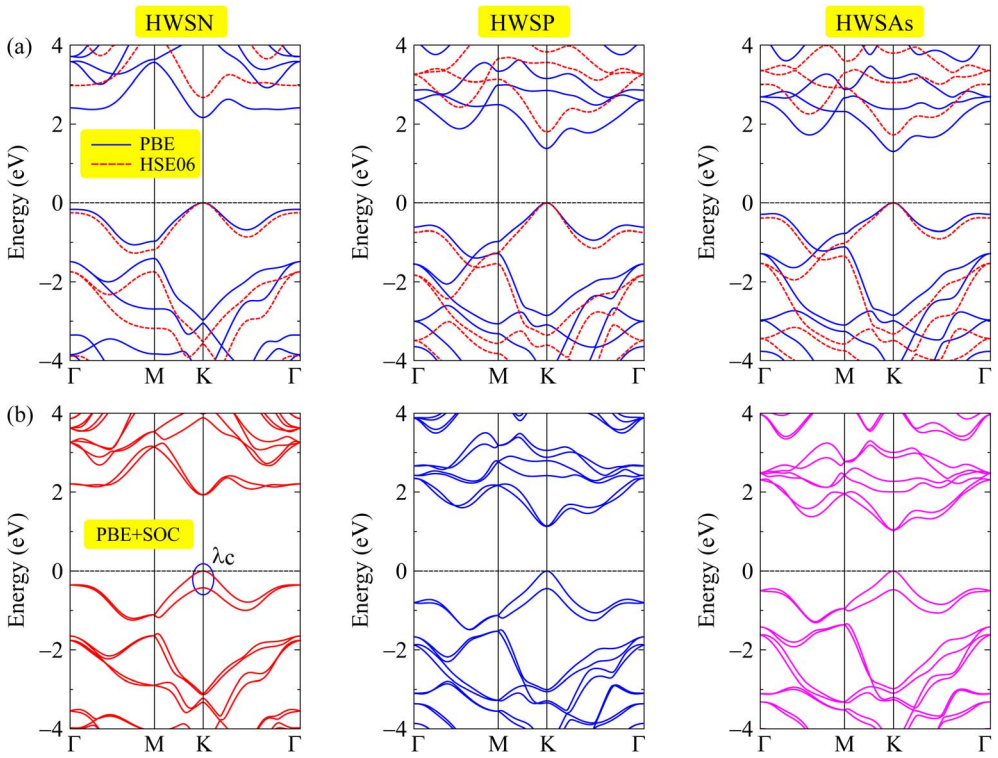


Fig. 5 Band structures of 2D Janus HWSZ (Z = N, P, As) monolayers at the PBE/HSE06 (a) and PBE + SOC (b) theoretical levels.

where $\mu_{ADP}$, $\mu_{IMP}$, $\mu_{PIE}$, and $\mu_{POP}$ refer to the carrier mobilities limited by ADP, IMP, PIE, and POP scattering, respectively.

The temperature dependence of the electron mobility in the Janus HWSZ monolayers is illustrated in Fig. 6. The two representative carrier concentrations $n_e$ of $1 \times 10^{16}$ and $1 \times 10^{20}$ $cm^{-3}$, correspond to the low and high carrier concentration regimes, respectively. When evaluating the volumetric carrier concentrations, the slab thickness of the HWSZ monolayers was

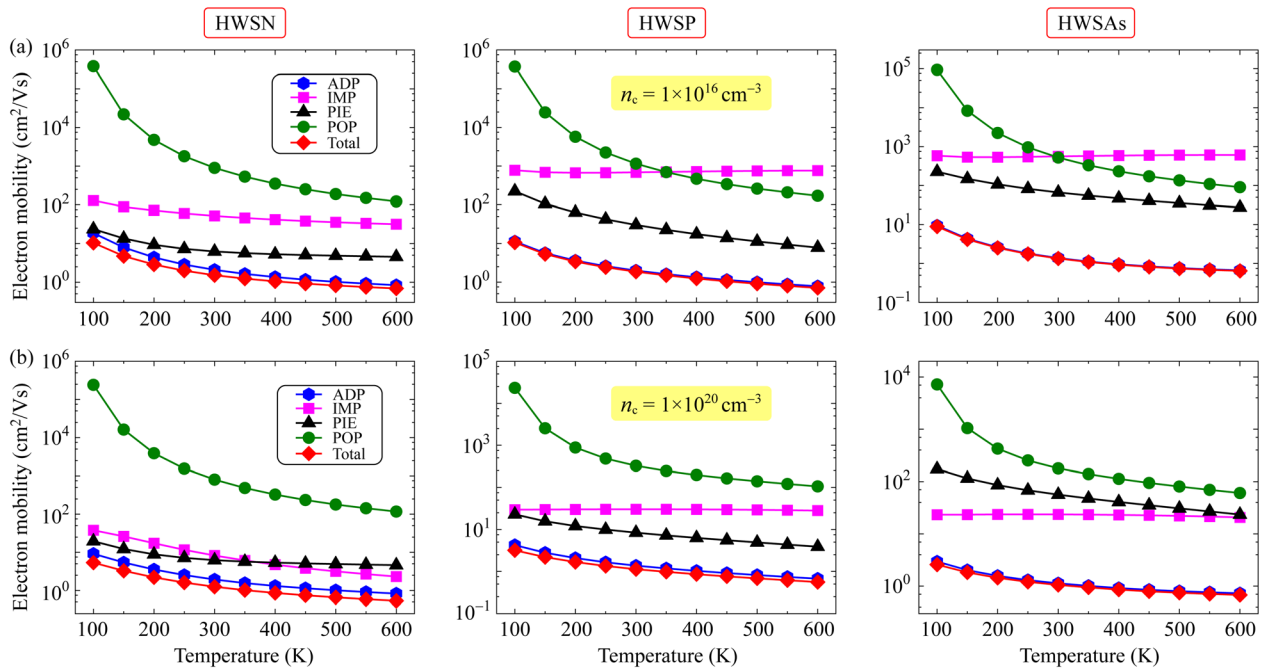


Fig. 6 Temperature dependence of individual and total electron mobilities in Janus HWSZ (Z = N, P, As) materials at carrier concentrations of $1 \times 10^{16}$ $cm^{-3}$ (a) and $1 \times 10^{20}$ $cm^{-3}$ (b).

defined as $\Delta h$ as listed in Table 1. This ensures the carrier concentration strictly reflects the volume of the 2D slab rather than the entire vacuum-padded simulation box. In both the low and high carrier concentration regimes, ADP scattering consistently acts as the primary mechanism governing the total electron mobility. This dominance is particularly evident in the HWSP and HWSAs monolayers, where the electron mobility limited by ADP scattering closely follows the trend of the total electron mobility over the entire temperature range, indicating that other scattering channels play only a minor role. In the meantime, for the Janus HWSN monolayer, the calculated results presented in Fig. 6 reveal a more complex interplay between scattering mechanisms. Although ADP scattering still provides a major contribution, PIE scattering also plays a non-negligible role in determining the overall magnitude of the total electron mobility, particularly in the low-temperature region. The comparable strength of these two mechanisms suggests that the intrinsic piezoelectric response of the HWSN monolayer enhances electron–phonon coupling through long-range polarization fields, thereby further limiting carrier transport. The dominant contribution of ADP scattering in the Janus HWSZ monolayers is consistent with that observed in the WBAsS[24] and $MoS_2$ or $WS_2$ monolayers.[19] Nevertheless, in the most 2D transition metal dichalcogenide materials, electron mobility is predominantly governed by longitudinal optical phonon scattering.[19] Even in $HfSiZ_3H$ monolayers,[4] which are structurally and chemically analogous to the materials studied in this study, POP scattering remains the governing factor. This highlights that scattering mechanisms in 2D materials are not easily predicted. A comprehensive analysis of all relevant scattering channels is therefore essential to accurately determine mobility limits.

Fig. 7 depicts the temperature dependence of hole mobility in the proposed Janus materials. Consistent with the behavior of electrons, APD scattering is the dominant mechanism governing total hole mobility, except for Janus HWSP monolayer, where PIE scattering becomes the dominant mechanism in the high-temperature regime. Furthermore, at high carrier concentration of $1 \times 10^{20}$ cm$^{-3}$, IMP scattering also plays a significant role in determining hole mobility within the HWSN monolayer, as depicted in Fig. 7(b). The competition between the IMP and PIE scattering mechanisms is similarly observable for electrons at high carrier concentration in this material, as shown in Fig. 6(b).

Table 3 presents a comprehensive summary of the carrier mobility in the Janus HWSZ monolayers at room temperature, including the individual contributions from different scattering mechanisms as well as the total mobility. The calculated results reveal that the electron mobility of the Janus HWSZ monolayers is relatively low. At a carrier concentration of $1 \times 10^{16}$ cm$^{-3}$, the room-temperature total electron mobilities $\mu_{tot}$ of HWSN, HWSP, and HWSAs are 10.45, 10.61, and 8.93 cm$^2$ V$^{-1}$ s$^{-1}$, respectively. As the carrier concentration increases, the mobility decreases markedly, indicating enhanced carrier scattering at higher doping levels. In the case of $n_c = 1 \times 10^{20}$ cm$^{-3}$, the room-temperature total electron mobilities of HWSN, HWSP, and HWSAs are reduced to 5.35, 3.19, and 2.58 cm$^2$ V$^{-1}$ s$^{-1}$, respectively. This same trend is clearly observable in the case of hole mobility, as detailed in Table 3. These results suggest that carrier transport in the Janus HWSZ monolayers is highly sensitive to doping levels, and optimizing carrier concentration will be essential for improving their electronic transport performance in practical device applications.

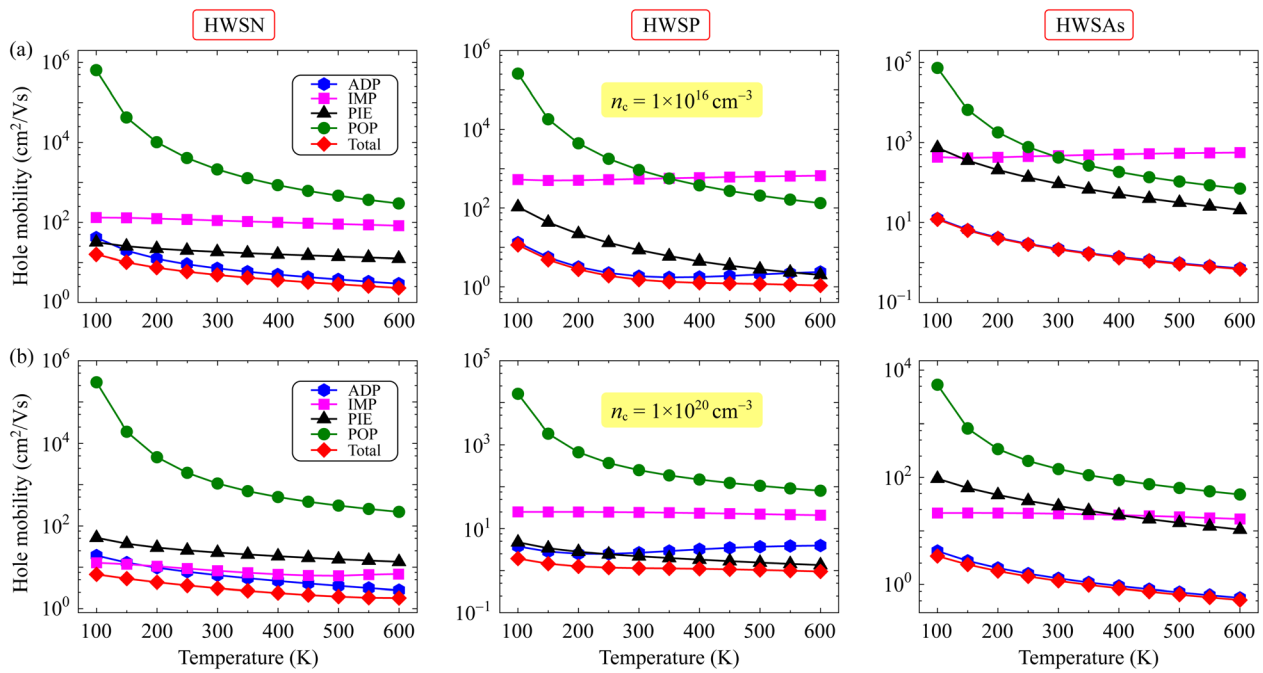


Fig. 7 Temperature dependence of individual and total hole mobilities in Janus HWSZ (Z = N, P, As) materials at carrier concentrations of $1 \times 10^{16}$ cm$^{-3}$ (a) and $1 \times 10^{20}$ cm$^{-3}$ (b).

Table 3 Room-temperature individual and total carrier mobilities ($\mu$, $cm^2 V^{-1} s^{-1}$) of Janus HWSZ (Z = N, P, As) at various carrier concentrations ($n_c$, $cm^{-3}$)

| Carrier type | Compound | $n_c$ | $\mu_{ADP}$ | $\mu_{IMP}$ | $\mu_{PIE}$ | $\mu_{POP}$ | $\mu_{total}$ |
|---|---|---|---|---|---|---|---|
| Electron | HWSN | $1 \times 10^{16}$ | 18.70 | $5.63 \times 10^8$ | 23.70 | $3.82 \times 10^5$ | 10.45 |
| | HWSP | | 11.30 | 776.00 | 223.00 | $3.71 \times 10^5$ | 10.61 |
| | HWSAs | | 9.45 | 581.00 | 226.00 | $9.33 \times 10^4$ | 8.93 |
| | HWSN | $1 \times 10^{20}$ | 9.14 | 37.90 | 19.50 | $2.41 \times 10^5$ | 5.35 |
| | HWSP | | 4.24 | 29.60 | 22.90 | $2.33 \times 10^4$ | 3.19 |
| | HWSAs | | 2.95 | 23.30 | 173.00 | $7.21 \times 10^3$ | 2.58 |
| Hole | HWSN | $1 \times 10^{16}$ | 7.16 | 111.00 | 18.20 | $2.12 \times 10^3$ | 4.90 |
| | HWSP | | 1.86 | 547.00 | 8.49 | 924.00 | 1.52 |
| | HWSAs | | 2.17 | 471.00 | 93.20 | 421.00 | 2.10 |
| | HWSN | $1 \times 10^{20}$ | 6.40 | 8.19 | 22.60 | $1.07 \times 10^3$ | 3.90 |
| | HWSP | | 2.65 | 24.40 | 2.19 | 248.00 | 1.14 |
| | HWSAs | | 1.30 | 21.00 | 29.20 | 143.00 | 1.17 |

# 4 Conclusion

In summary, DFT calculations confirm that Janus HWSZ (Z = N, P, As) monolayers are stable, direct-gap semiconductors with high experimental viability. Their broken inversion symmetry, combined with strong spin–orbit coupling (SOC), induces massive spin splitting, positioning these materials as premier candidates for spintronic devices. However, transport analysis indicates that electron mobility in HWSZ is relatively low and fundamentally limited by ADP scattering. Despite these transport limitations, the pronounced out-of-plane piezoelectric response offers a viable route toward multifunctional electromechanical integration. Ultimately, the combination of sizable band gaps, strong spin splitting, and robust piezoelectricity establishes HWSZ monolayers as a versatile platform for next-generation nanoelectronic applications, provided that their intrinsic scattering mechanisms are carefully controlled.

# Conflicts of interest

There are no conflicts of interest to declare.

# Data availability

The data that support the findings of this study are available from the authors upon reasonable request.

# References

1 J. Zhang, S. Jia, I. Kholmanov, L. Dong, D. Er, W. Chen, H. Guo, Z. Jin, V. B. Shenoy, L. Shi and J. Lou, *ACS Nano*, 2017, **11**, 8192–8198.
2 A.-Y. Lu, H. Zhu, J. Xiao, C.-P. Chuu, Y. Han, M.-H. Chiu, C.-C. Cheng, C.-W. Yang, K.-H. Wei, Y. Yang, Y. Wang, D. Sokaras, D. Nordlund, P. Yang, D. A. Muller, M.-Y. Chou, X. Zhang and L.-J. Li, *Nat. Nanotechnol.*, 2017, **12**, 744.
3 M. Yagmurcukardes, Y. Qin, S. Ozen, M. Sayyad, F. M. Peeters, S. Tongay and H. Sahin, *Appl. Phys. Rev.*, 2020, **7**, 011311.
4 T. V. Vu, N. T. Hiep, H. V. Phuc, B. D. Hoi, A. I. Kartamyshev and N. N. Hieu, *Phys. Rev. B*, 2024, **110**, 235403.
5 M. Yao, J. Chen, X. Cai, Y. Tang, Y. Ni, C. Guo, H. Wang, B. Sun and Y. Chen, *ACS Appl. Nano Mater.*, 2024, **7**, 7773–7782.
6 N. T. Hiep, C. Q. Nguyen, C. V. Nguyen, T. V. Vu and N. N. Hieu, *Phys. Rev. B*, 2025, **112**, 045431.
7 X. Yue, Y. Xia, D. Ding, W. F. IO, D. He, C. He, Y. Wang, H. Xue, Y. Jin, M. Yuan, J. Zhang, W. Ho, H. Xu, D.-K. Ki, J. Hao, C. Jin and M. Xie, *2D Mater.*, 2025, **12**, 025004.
8 S. N. Reed-Lingenfelter, M. Wang, N. L. Williams and J. J. Cha, *Adv. Mater. Interfaces*, 2021, **9**, 2100463.
9 J. H. Jeong, S. Kang, N. Kim, R. Joshi and G.-H. Lee, *Phys. Chem. Chem. Phys.*, 2022, **24**, 10684–10711.
10 L. Zhang, J. Yu, M. Yang, Q. Xie, H. Peng and Z. Liu, *Nat. Commun.*, 2013, **4**, 1443.
11 P. E. Blöchl, *Phys. Rev. B: Condens. Matter Mater. Phys.*, 1994, **50**, 17953.
12 G. Kresse and D. Joubert, *Phys. Rev. B: Condens. Matter Mater. Phys.*, 1999, **59**, 1758–1775.
13 J. P. Perdew, K. Burke and M. Ernzerhof, *Phys. Rev. Lett.*, 1996, **77**, 3865.
14 J. Heyd, G. E. Scuseria and M. Ernzerhof, *J. Chem. Phys.*, 2003, **118**, 8207.
15 A. H. MacDonald, W. E. Picket and D. D. Koelling, *J. Phys. C: Solid State Phys.*, 1980, **13**, 2675.
16 A. Togo, L. Chaput and I. Tanaka, *Phys. Rev. B: Condens. Matter Mater. Phys.*, 2015, **91**, 094306.
17 M. Yagmurcukardes, F. M. Peeters and H. Sahin, *Phys. Rev. B*, 2018, **98**, 085431.
18 A. M. Ganose, J. Park, A. Faghaninia, R. Woods-Robinson, K. A. Persson and A. Jain, *Nat. Commun.*, 2021, **12**, 2222.
19 L. Cheng and Y. Liu, *J. Am. Chem. Soc.*, 2018, **140**, 17895–17900.
20 R. H. J. Vervuurt, B. Karasulu, M. A. Verheijen, W. E. M. M. Kessels and A. A. Bol, *Chem. Mater.*, 2017, **29**, 2090–2100.
21 M. Born and K. Huang, *Am. J. Phys.*, 1955, **23**, 474.
22 F. Mouhat and F.-X. Coudert, *Phys. Rev. B: Condens. Matter Mater. Phys.*, 2014, **90**, 224104.

23 T. V. Vu, B. D. Hoi, A. I. Kartamyshev and N. N. Hieu, *J. Appl. Phys.*, 2024, **135**, 074301.
24 T. V. Vu, L. V. Hung, C. V. Nguyen, N. T. Hiep, K.-M. Bui, A. I. Kartamyshev and N. N. Hieu, *Appl. Phys. Lett.*, 2025, **127**, 081601.
25 O. Leenaerts, H. Peelaers, A. D. Hernández-Nieves, B. Partoens and F. M. Peeters, *Phys. Rev. B: Condens. Matter Mater. Phys.*, 2010, **82**, 195436.
26 K.-A. N. Duerloo, M. T. Ong and E. J. Reed, *J. Phys. Chem. Lett.*, 2012, **3**, 2871–2876.
27 Y. Guo, S. Zhou, Y. Bai and J. Zhao, *Appl. Phys. Lett.*, 2017, **110**, 163102.
28 S.-D. Guo, W.-Q. Mu, Y.-T. Zhu, R.-Y. Han and W.-C. Ren, *J. Mater. Chem. C*, 2021, **9**, 2464–2473.
29 X. Cai, G. Chen, R. Li, Z. Pan and Y. Jia, *J. Mater. Chem. C*, 2024, **12**, 4682–4689.
30 S.-D. Guo, Y.-T. Zhu, K. Qin and Y.-S. Ang, *Appl. Phys. Lett.*, 2022, **120**, 232403.